Finite-Element Calculations of the Lattice Rotation Field of a Tensile-Loaded Nickel-Based Alloy Multicrystal and Comparison with Topographical X-Ray Diffraction Measurements

F. EBERL, S. FOREST, T. WROBLEWSKI, G. CAILLETAUD, and J.L. LEBRUN

A new experimental measurement technique using synchrotron radiation is applied to determine the curvature of the crystallographic lattice within a grain of a multicrystalline specimen after uniaxial tensile loading. The experimental results are compared to a three-dimensional finite-element model, which is based on a classical crystal-plasticity law. The model takes the entire microstructure of the multicrystal into account. A small-strain and small-rotation formalism allows calculation of the orientation matrix at each integration point for each deformation step. A good agreement of the experimental and numerical data has been found. The experimental technique is based on image-data processing. The development of data-treatment algorithms allows distinction to be made between the regular crystallographic curvature and the random mosaic distribution always present in polycrystalline materials.

I. INTRODUCTION

IN the description of the mechanical behavior of polycrystalline materials, homogenization approaches are often used to predict the macroscopic properties.[1] According to the so-called self-consistent scheme, for instance, one computes the interaction between different phases in an unlimited area. However, parameters such as grain size and transgranular stress and strain heterogeneities are not taken into account.

In the following article, a finite-element approach with a crystal-plasticity model at each integration point is used.[2,3] Thanks to the introduction of finite elements at the grain scale, the grain size and its morphology become an additional parameter in the description of the mechanical behavior of a polycrystal. In order to describe the entire microstructure of a sample, a multicrystalline microstructure is considered. The word multicrystal, instead of polycrystal, denotes a sample with a small number of large grains (Figure 1). The chosen material is the nickel-based INCO600,* a solid-solution-strengthenedalloy.[4] It has been heat-treated in order to obtain large recrystallized grains. The specimen studied in this work, represented in Figure 1, contains a small number of grains across the sample thickness, so that an entire meshing of the microstructure is possible. A flat sample with five grains in the gage area is considered, under tensile loading conditions at room temperature. Under these conditions, only octahedral slip was expected and was, in fact, observed.

*INCO is a trademark of INCO Alloys International, Huntington, WV.

The validation of the model has to be done on the grain scale and on the macroscopic scale of the entire sample. In Reference 5, the transgranular stress field was evaluated using an X-ray microbeam technique. The stress tensor could be determined at different locations within the grain and compared to the numerically calculated transgranular stress field.

In the present study, the evolution of the crystallographic orientation within the grain is of interest. The introduction of a small-strain and small-rotation formalism is sufficient to calculate the lattice orientation at each integration point for each loading step, for the investigated range of tensile loading conditions.

Generally, for the experimental analysis of stress and strain heterogeneities on the transgranular scale, the beam size determines the resolution within the grain. In Reference 5, a 150-μm-wide beam is used for the local stress determination in a multicrystalline sample with grain sizes between 1 and 5 mm. In the present work, a very wide beam, which covers the entire grain, interacts with the sample. In order to detect the scattered signal of the entire grain, a two-dimensional detector is used, where the size of the pixel dictates the detector resolution. For the experimental determination of lattice rotation, an X-ray imaging technique has been developed at the G3 beamline of the synchrotron facility in the HASYLAB. The basic idea is the acquisition of an entire grain in its reciprocal space, thanks to a two-dimensional detection. The use of a highly sensitive close-coupled device (CCD) camera allows identification of each pixel on the acquired image with a material point on the sample. The development of an image data-treatment software allows transformation of large amounts of acquired data into the desired mechanical variables such as the elastic strain and the lattice orientation, which can directly be compared with the results obtained by the finite-element simulation.

In comparison to the recent developments in the electron back-scattering pattern (EBSP) analysis used in scanning

F. EBERL, formerly Doctor with LM3, Ecole Nationale Supérieure d'Arts et Métiers Paris, 78013 Paris, France, is Research Engineer, Pechiney-CRV, 38340 Voreppe, France. S. FOREST, Researcher, and G. CAILLETAUD, Professor, are with the Centre des Matériaux, Ecole des Mines de Paris, 91003 Evry Cedex, France. Contact e-mail: Samuel.forest@mat.ensmp.fr T. WROBLEWSKI, Professor, is with DESY-HASYLAB, D-22603 Hamburg, Germany. J.L. LEBRUN, formerly Doctor with LM3, Ecole Nationale Supérieure d'Arts et Métiers Paris, is Professor, LPMI, Ecole Nationale Supérieure d'Arts et Métiers Angers, 49100 Angers, France.

Manuscript submitted June 12, 2001.

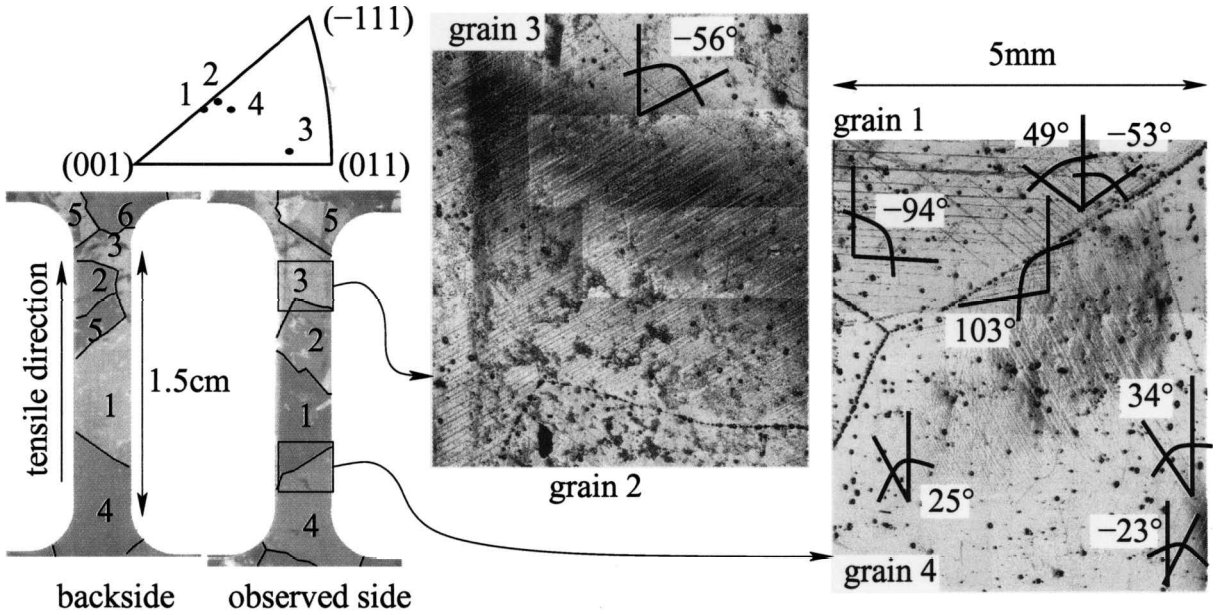

Fig. 1—Microstructure of the multicrystal specimen with the orientation distribution of four main grains. Micrograph of grain 1 and 4 with observation of slip lines. The scale 5 mm is valid for both grain 1/4 and 2/3.

electron microscopy,[6] the advantage of the X-ray measurement technique is the lower sensitivity to the sample surface quality and the simultaneous acquisition of the local elastic strain and the lattice orientation of the grain. Only the lattice orientation field is studied in this work. The combination of finite-element computations and systematic EBSP mapping has been used in the past for the analysis of the deformation modes in metallic multicrystals.[7,8] The present work, therefore, is a validation of the new X-ray orientation imaging technique. The lattice orientation may vary from point to point within a grain, for different reasons. A random distribution of low-angle grain boundaries, called mosaicity, exists in the initial undeformed grain. Deformation of the grain leads to a smoother variation of the mean local orientation, called lattice curvature, associated with deformation gradients. The proposed method is able to determine both kinds of maps, as will be shown in this work. In contrast, the simulation does not take the initial mosaicity into account. That is why the present works focuses on the determination of the lattice curvature field after straining.

This article is organized as follows. The crystal-plasticity model used is recalled in the first section, with special focus on lattice rotation. The second section is devoted to the experimental procedure designed for measuring lattice rotation fields. The third part deals with the description of the geometry of the investigated multicrystalline specimen and of the formation of slip lines in the grains during tensile loading. In the final discussion, all experimental results are compared with the predictions of the finite-element analysis.

II. CRYSTAL-PLASTICITY MODEL

The crystal-plasticity constitutive model used in the present work was originally formulated in Reference 2, within the small-strain framework. The main equations are recalled in Section II–A. However, for the strain range considered in the present application, it is necessary to take lattice rotation explicitely into account. This is done in Section II–B.

A. *Constitutive Equations*

The total-strain tensor can be decomposed into an elastic and a viscoplastic part:

$$= {}^{e} + {}^{p} \qquad [1]$$

Hooke's law relates the elastic strain to the stress tensor. An elasticity tensor with cubic symmetry is used in this work. The plastic deformation is the sum of glide processes (γ^g) according to N slip systems specific of the considered crystal structure. The vectors $\mathbf{n}^g$ and $\mathbf{m}^g$ denote, respectively, the normal to the slip plane and glide direction of slip system g:

$${}^{p} = \sum_{g=1}^{N} \gamma^g \, (\mathbf{m}^g \otimes \mathbf{n}^g + \mathbf{n}^g \otimes \mathbf{m}^g)/2 \qquad [2]$$

The activation of slip system g is predicted by the Schmid law, *i.e.*, when the resolved shear stress (τ^g) reaches a threshold value (r^g):

$$\tau^g = \mathbf{m}^g \cdot \boldsymbol{\sigma} \cdot \mathbf{n}^g = r^g, \text{ for } g = 1, \ldots, N \qquad [3]$$

The amount of plastic slip is computed *via* a viscoplastic flow rule:

$$\gamma^g = \left\langle \frac{|\tau^g - x^g| - r^g}{k} \right\rangle n \text{ sign } (\tau^g - x^g) \qquad [4]$$

$$\text{with } \langle a \rangle = \begin{cases} a & \text{if } a > 0 \\ 0 & \text{if } a \le 0 \end{cases}$$

Internal variables of isotropic and kinematic hardening (τ^g and x^g, respectively) have been introduced for each slip system g. Their nonlinear evolution rules are given by the following equations:

Table I. Model Parameters

Elastic Coefficients of the Nickel Single Crystal at Room Temperature		
C11 in MPa	C12 in MPa	C44 in MPa
248,100	154,900	124,200

Inelastic coefficients for the Heat-Treated Nickel Based Alloy							
k ($MPa^{1/n}$)	n	c (MPa)	d	r_0 (MPa)	q (MPa)	b	h_{ij}
25	12	16,000	1500	18	3	10	1

$$r^g = r_0 + q\sum_{r=1}^{N} h^{gr}\,(1 - e^{-bv^r}),\ \text{with}\ v^g = \left|\gamma^g\right| \qquad [5]$$

$$x^g = c\alpha^g,\ \text{with}\ \alpha^g = \gamma^g - d\left|\gamma^g\right|\alpha^g \qquad [6]$$

The investigated material has an fcc crystal structure, and the observed systems belong to the octahedral family ($\{111\}\langle 011\rangle$, $N = 12$ slip systems). The model involves seven material parameters: n, k, d, c, r_0, q, b. These have been identified on the grain scale by using microstrain gages covering the entire grain surface and X-ray diffraction measurements of the elastic strain in a multicrystalline sample. At several loading stages, the local total strain and the local stress were determined, so that a stress-strain curve at a second-order scale could be obtained. The numerical stress-strain curve of the same grain was fitted to the experimental one to determine the seven material parameters. This calibration procedure has been done with a specimen different from the multicrystal considered in this work. It is described in detail in Reference 5. The hardening matrix (h^{gr}) is assumed to be isotropic, with equivalent self- and latent hardening for all slip systems. The values of the material parameters used in this work are given in Table I.

B. *Introduction of Lattice Rotations*

In the present study, we want to compare lattice curvature measurements with simulations; therefore, it is necessary to include lattice rotations in the model. A comprehensive treatment of lattice curvature and its relation to plastic deformation and, especially, strain localization can be found in Reference 9. In the following text, the finite-deformation crystal-plasticity framework is briefly recalled. A detailed presentation of the large-deformation theory of single crystals and some applications can be found, for instance, in References 10 through 14. The partition of the total deformation gradient ($\mathbf{F}$) into elastic and plastic parts is based on the introduction of an intermediate stress-released configuration, leading to a multiplicative decomposition:

$$\mathbf{F} = \mathbf{E}\cdot\mathbf{P} \qquad [7]$$

This intermediate, so-called isoclinic configuration is such that the crystal orientation with respect to the laboratory axes is the same as the initial one. This takes into account the fact that purely plastic deformation does not affect the crystal lattice. The current orientation of the lattice directions with respect to the initial one is then determined by the rotation in the polar decomposition of the elastic part of deformation:[15]

$$\mathbf{E} = \mathbf{S}^e\cdot\mathbf{R}^e \qquad [8]$$

where $\mathbf{S}^e$ is the symmetric positive definite and $\mathbf{R}^e$ is a rotation.

In the model used in References 2, 3, and 16, lattice rotations are not taken into account. The crystal orientation was kept constant throughout the whole simulation. If experimental results only deal with relatively small amounts of strain, lattice rotations do not significantly affect the results concerning the evolution of the viscoplastic strain and stress distribution.[17] In the present study, this remark has been confirmed by equivalent simulations, one with and one without lattice rotations.[3] That is why it is sufficient to consider here a small-strain and small-rotation formulation. It can be deduced from the previous general crystal-plasticity theory as follows. If strains and rotations remain small throughout the test, the previous decompositions reduce to

$$\begin{aligned}\mathbf{F} &= \mathbf{S}^e\cdot\mathbf{R}^e\cdot\mathbf{P}\\ &\simeq (\mathbf{1} + \ ^e)\cdot(\mathbf{1}+\boldsymbol{\omega}^e)\cdot(\mathbf{1} + \ ^p + \boldsymbol{\omega}^p)\\ &\simeq \mathbf{1} + \ ^e + \boldsymbol{\omega}^e + \ ^p + \boldsymbol{\omega}^p\end{aligned} \qquad [9]$$

where symmetric and skew-symmetric parts of all tensors have been introduced and quadratic terms have been neglected. Accordingly, the velocity gradient takes the simple form of

$$\mathbf{F}\cdot\mathbf{F}^{-1} \simeq \ ^e + \boldsymbol{\omega}^e + \ ^p + \boldsymbol{\omega}^p = \ + \boldsymbol{\omega} \qquad [10]$$

with $\ = \ ^e + \ ^p$ and $\boldsymbol{\omega} = \boldsymbol{\omega}^e + \boldsymbol{\omega}^p$. The plastic-deformation and rotation rates are then given by

$$^p = \frac{1}{2}\sum_{g=1}^{N}\gamma^g\,(\mathbf{m}^g\otimes\mathbf{n}^g + \mathbf{n}^g\otimes\mathbf{m}^g) \qquad [11]$$

$$\boldsymbol{\omega}^p = \frac{1}{2}\sum_{g=1}^{N}\gamma^g\,(\mathbf{m}^g\otimes\mathbf{n}^g - \mathbf{n}^g\otimes\mathbf{m}^g) \qquad [12]$$

Finally, the slip-plane normal vector and the slip direction are updated as follows:

$$\mathbf{m}^g = \boldsymbol{\omega}^e\cdot\mathbf{m}^g,\ \mathbf{n}^g = \boldsymbol{\omega}^e\cdot\mathbf{n}^g \qquad [13]$$

These expressions are valid for a small-strain and small-rotation framework only. The advantage of this formulation is numerical efficiency, because the geometric nonlinearity of the problem is reduced. It has been confirmed that this small-strain and small-rotation framework remains accurate up to 10 pct plastic slip.

III. EXPERIMENTAL DETERMINATION OF THE CRYSTALLOGRAPHIC LATTICE ORIENTATION

The objective of the study is the determination of lattice rotation maps in a given grain, using synchrotron radiation. For that purpose, a large incident beam covering the entire grain is used. Due to the low divergence (0.9×0.4 mrad) and the power of the incident beam, the synchrotron radiation facility at DESY Hamburg was chosen as a well-suited tool. Thanks to the parallel beam, the diffraction angles are conserved. It is, therefore, possible to analyze a large scattering zone (5×5 mm). Details on the experimental setup are given in Section III–A. Section III–B deals with the data collection: intensity as a function of the angles (θ, Ω, and

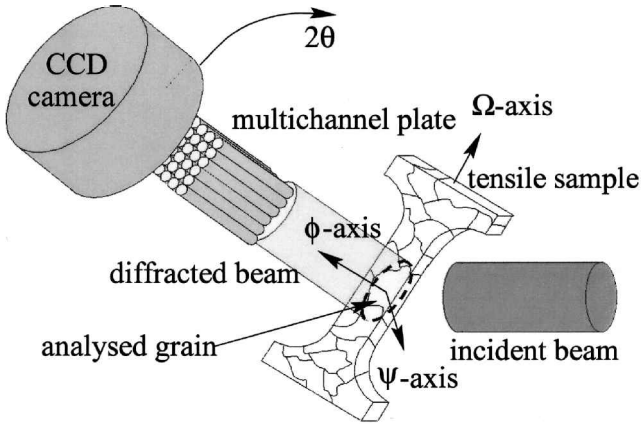

Fig. 2—Experimental setup of the G3 beamline at HASYLAB.

Ψ) defined in Figure 2. Section III–C describes the algorithm giving the final orientation map of the grain.

A. *Experimental Setup*

The experimental apparatus is sketched in Figure 2. It consists of several parts.

(1) A four-circle goniometer. The Φ and Ψ angles can be considered as the spherical coordinates of the diffracting plane. In the sequel, we use the angle Ω instead of Φ, which gives an equivalent description of the plane orientation. According to Bragg's law, $\lambda = 2d_{hkl} \sin \theta$, where λ is the wave length, d is the lattice distance of the considered crystallographic planes $\{hkl\}$, and the detector is fixed on the Bragg-angle position around the θ axis.
(2) A large incident beam. The beam size is about 5 × 5 mm. The chosen wave length was 0.9 A, so that the high-multiplicity plane family {531} could be observed at a Bragg angle of 52 deg.
(3) A multichannel plate: 1000 × 1000 microtubes, with a length of 1 cm and a diameter of 10 μm. A radial resolution of 1 mrad can be obtained.
(4) A CCD camera as a detector, with a resolution of 1000 × 1018 pixels (pixel size: 12 × 12 μm). The detector is located as close as possible to the sample (about 5 cm away).

A compromise has to be found between the diffraction condition (Bragg angle of the observed crystallographic plane corresponding to the wave length used) and the optically best orientation of the sample surface to the detector surface.

B. *Data Acquisition*

For a fixed angle of Ψ, a reciprocal-space map is acquired, as shown in Figure 3. At each (Ω, θ) position, the intensity of the scattered beam at each pixel (i, j) is recorded. Each pixel (i, j) is associated with a material point in the analyzed grain. An interval of 0.5 deg for 2θ is investigated, with $m = 25$ steps. The $n = 20$ values of Ω are distributed over an interval of 2 deg. This requires the storage of 20 × 25 images.

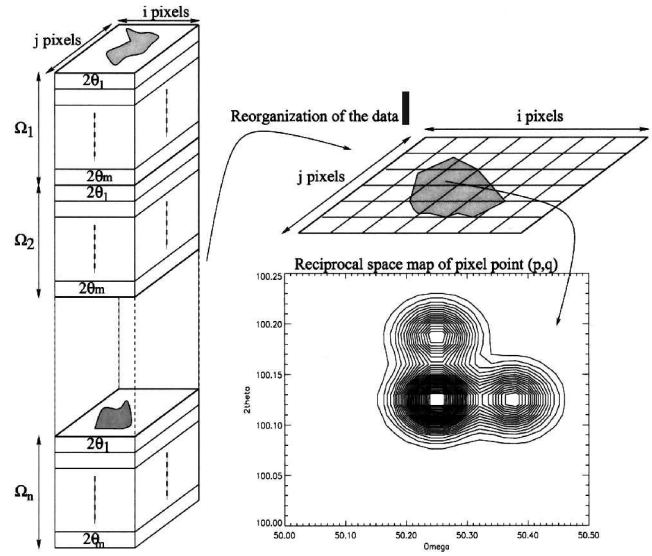

Fig. 3—Principle of the reorganization of data for a reciprocal space acquisition using an imaging method. The gray spots correspond to the part of the grain that is well oriented for diffraction for the specific values (Ψ_i, Ω_j, θ_k).

In order to obtain an image of the entire grain, the reciprocal-space map has to be repeated for several Ψ orientations. Figure 4 shows an example of five Ψ angles with a difference of $\Delta\Psi = 0.3$ deg. Different zones in the grain (marked in black in the figure) may be well oriented for diffraction. The total of these five Ψ positions already covers a large part of the grain. The total analysis of one single grain lasts about 2 hours. Smaller step sizes and a larger investigated range for Ψ would be necessary to image a larger part of the grain. This requires, however, a larger storage capacity and longer acquisition time.

C. *Data Analysis*

The data must now be reorganized so that a reciprocal-space map is obtained for each pixel.[18] The acquired images must be stacked, and rods have to be cut out of the stack as illustrated in Figure 3. This is done for all Ψ angles for one crystallographic measurement direction [*hkl*]. The final images for each Ψ angle are summed up to one final representative image for this specific measurement direction. The sum of all Ψ angles leads to the almost-complete representation of the grain, shown on the right-hand side of Figure 4.

The last step is the processing of the data of the reciprocal-space map. Generally, a two-dimensional peak, which is not always symmetric, is observed. In order to determine the lattice parameter, the peak position of the diagonal cut Ω-2θ of the reciprocal-space map must be determined.

Figure 5 shows the example of reciprocal-space maps of a given pixel before and after plastic straining of the grain. It can be observed that the peak is broadened after deformation, especially in the Ω direction. Two methods for determining the peak location were used: the center of gravity and the two-dimensional Gauss fit, which allows the use of the peak width at half height:

$F(\Omega, \theta) = A_0 + A_1 e^{-\frac{U}{2}}$, with the elliptical function U

$$= \left(\frac{\Omega - \Omega_0}{a}\right)^2 + \left(\frac{\theta - \theta_0}{b}\right)^2 \quad [14]$$

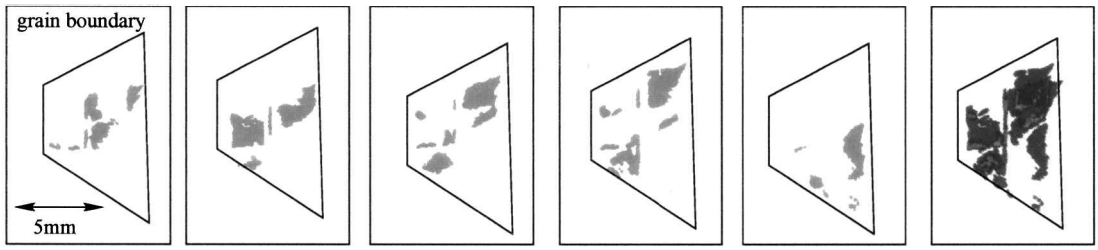

Fig. 4—Diffracting volumes of the grain for five different Ψ orientations (for a given pair (Ω, θ)). The trapezoidal shape represents grain 1. The shaded zones within the grain are well oriented for diffraction. The last picture on the right gives the total investigated part of the grain for all five Ψ orientations.

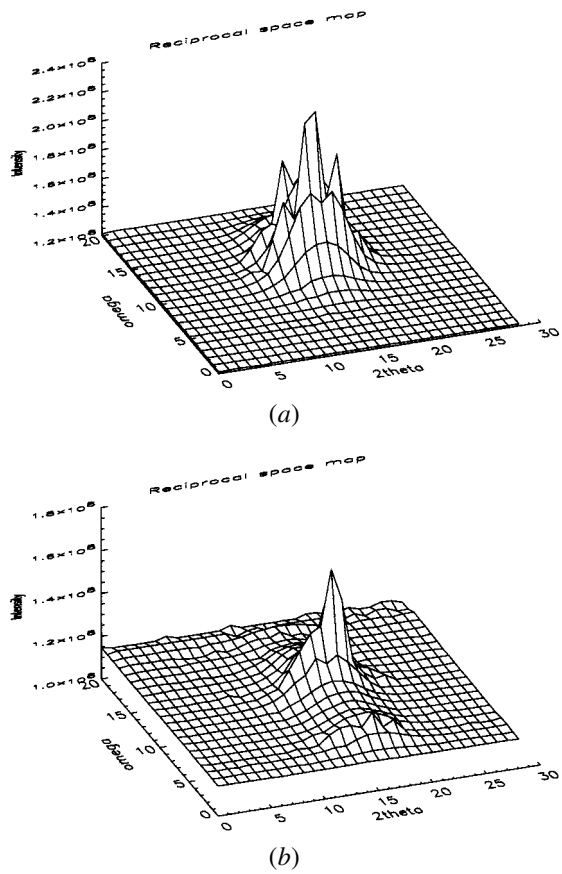

Fig. 5—Reciprocal space mapping at (*a*) initial and (*b*) strained states of peak {3$\bar{5}$1}.

The characteristic parameters of the Gauss approximation are

A_0 = constant term,
A_1 = scale factor,
a = width of Gaussian curve in the Ω direction,
b = width of Gaussian curve in the 2θ direction,
Ω_0 = center of the Ω location,
θ_0 = center of the 2θ location.

Thanks to this new measurement technique, it is now possible to acquire reciprocal-space maps for each "subgrain," represented as a pixel, of a grain in a multicrystalline matrix. The peak position of the Ω-2θ scan represents the stress state of the "pixel," so that entire stress maps of the grain can be acquired. The Ω position represents the orientation of the scattering vector. The Ω angle can be compared directly to the orientation of the crystallographic lattice calculated by the finite-element model. This is done in Section V.

IV. PRESENTATION OF THE MULTICRYSTALLINE SPECIMEN: MECHANICAL TESTING AND FINITE-ELEMENT ANALYSIS

A. *Geometry of the Grains and Corresponding Finite-Element Mesh*

In order to be able to model the entire microstructure of a tensile sample, a polycrystal is introduced with a low number of grains. Accordingly, the grain morphology is known even in the thickness of the sample. A heat treatment of 140 hours at 1300 °C of the nickel-based 600 alloy initiated grain growth, so that a microstructure, as presented in Figure 1, could be obtained. It turns out that grain 3 does not completely fill the cross section of the specimen. However, the observation of both lateral surfaces of the sample leads to an accurate description of the morphology of grains 2 and 3.

The knowledge of the geometry of the individual grains makes it possible to design a finite-element mesh that follows the grain boundaries. The crystallographic orientation of all individual grains has been measured by X-ray analysis. These orientations are explicitely taken into account in the simulation. The finite-element mesh of the sample considered in this work contains 1200 quadratic bricks, with three layers of elements in the thickness. Each element has 20 nodes and 27 integration points, which represents a resolution of 200 μm per integration point. In order to reproduce the real microstructure as closely as possible, both sides of the sample are meshed following the real grain boundaries. Both sides contain the same number of elements per grain, so that it is possible to simulate tilted grain boundaries in the thickness of the sample. There may be, sometimes, two grains in the thickness (grains 2 and 5, for instance), as can be seen from Figure 1. The mesh is fine enough to take this into account. The number of elements allows calculations in a sequential mode on a single workstation.

B. *Deformation of the Multicrystal: Experimental Observations*

A tensile test was performed on the sample at room temperature, up to 2 pct overall strain. The activated slip systems and the corresponding lattice rotations were analyzed. Note

Table II. Theoretical Angles between the Tensile Axis and the Slip Plane with the Corresponding Schmid Factors

	$(1\bar{1}1)$			$(11\bar{1})$			$(\bar{1}11)$			(111)		
	$[10\bar{1}]$	[110]	[011]	[101]	[011]	$[1\bar{1}0]$	[101]	$[0\bar{1}1]$	[110]	$[10\bar{1}]$	$[0\bar{1}1]$	$[1\bar{1}0]$
Grain 1	0.0	0.19	0.19	0.20	0.45	0.25	0.21	0.25	0.46	0.0	0.39	0.40
		13 deg			−92 deg			54 deg			−58 deg	
Grain 2	0.31	0.08	0.39	0.40	0.20	0.20	0.13	0.12	0.01	0.21	0.47	0.26
		−13 deg			71 deg			32 deg			−53 deg	
Grain 3	0.31	0.31	0.13	0.35	0.0	0.47	0.07	0.13	0.08	0.04	0.08	0.06
		59 deg			−60 deg			84 deg			6 deg	
Grain 4	0.32	0.08	0.39	0.40	0.20	0.20	0.13	0.12	0.01	0.21	0.47	0.26
		100 deg			28 deg			45 deg			36 deg	

that it was not an *in-situ* test, so that lattice orientation fields were measured only after the test.

During plastic deformation, slip lines appear, depending on the activated slip systems. The slip lines can be observed with an optical microscope. Each line corresponds to the intersection of a cluster of parallel active slip planes with the observed sample surface. Following Schmid's law, the theoretical slip-line angles can be calculated. The grain is considered as a single crystal, and the slip systems with the highest Schmid factor are given in Table II. These angles have to be compared with the measured angles shown in Figure 1. The Schmid factor (*i.e.*, $\cos\phi \times \cos\psi$, with a ϕ-angle slip-direction–tensile axis and ψ-angle plane normal–tensile axis) is computed using the orientation of the slip plane and slip direction with respect to the tensile axis. In the case of a uniaxial loading, the slip systems with the highest Schmid factor go first into the plastic regime. In the present case, even if the loading state at the grain scale is not completely uniaxial, the Schmid factor is a good indicator of the sensitivity of the activated slip systems. Due to the mosaicity, which provokes local variations of the orientation matrix, and to the accuracy of the experimental-angle determination, an accuracy of ±5 deg is accepted.

Grains 1 and 2 are found to be stiffer than grains 3 and 4, which can be explained by their respective orientations (refer to the inverse pole figure of the tensile axis in Figure 1). Even if grains 1 and 2 have very close crystallographic orientations, their mechanical behavior in the multicrystal is very different. Double slip is observed in grain 1, rather homogeneously over the whole grain. In contrast, grain 2 does not show slip traces during the entire tensile test. Grain 2 is neighboring with grain 3, which shows intense slip traces. In grain 3, even in the perpendicular direction to the sample surface a rather large strain can be noticed. The measured angle of the single-slip traces is −56 deg (theoretical: −60 deg for slip system $(111)[1\bar{1}0]$), which corresponds rather well to the theoretical calculation of the slip system with the highest Schmid factor. Grain 1 is rather homogeneously plastically deformed, with a higher number of activated slip systems close to the grain boundaries. The slip lines of the primary slip system with the angle of 49 deg (theoretical: 54 deg for slip system $(\bar{1}11)[110]$) are denser near the boundary with grain 4. The secondary slip system $(11\bar{1})[011]$, with the angle of −94 deg (theoretical: −92 deg) is slightly lower near the grain boundary, as is also confirmed by the model. The higher-order slip of angle −53 deg (theoretical: −58 deg for slip system $(111)[1\bar{1}0]$) is activated close to the grain boundary with grain 4.

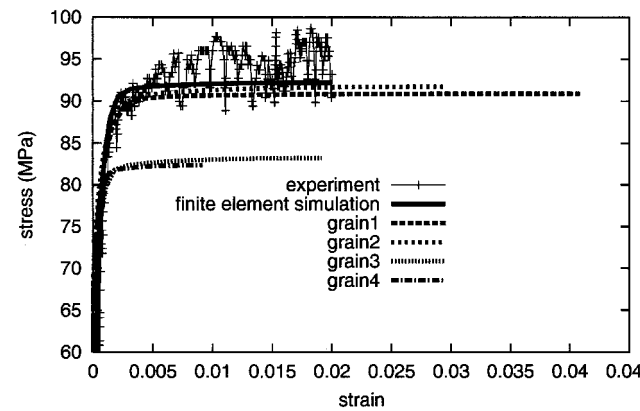

Fig. 6—Overall stress-strain curve for the tension of a multicrystalline specimen. It is compared to the corresponding curve predicted by the finite-element analysis. Computed mean stress and strain values in four grains are also given for comparison: grains 1 and 2 (3 and 4, respectively) display a similar stress state but different strain states.

Strain localization appears in grain 4. A diagonal deformation band crosses the entire section of the grain and the tensile sample. The highest Schmid factor corresponds to a slip line with a theoretical angle of 36 deg, which is still in the tolerated interval if one looks at the measured 34 deg angle of the same slip system close to the specimen edge.

It can be concluded that the main deformation mechanism is represented by one or two slip systems activated over the entire grain. These main slip systems correspond to the highest Schmid factors calculated if the grain were a single crystal. In order to accommodate strain incompatibilities, higher-order slip systems are activated close to the grain boundary, which indicates a locally multiaxial stress state.

C. *Finite-Element Simulation of the Tensile Test*

The finite-element mesh of the entire multicrystalline sample designed in Section IV–A is used to simulate the previous tensile test. Displacement is prescribed at the top and bottom to reach a 2 pct overall strain. Due to the inhomogeneity of grain orientations, nonhomogeneous stress-strain fields arise. The computation can provide overall curves and mean values, on the one hand, and the local stress-strain fields, on the other hand. The overall stress-strain curve is given in Figure 6 and compared to the experimental one. Note that these curves are rather flat in comparison to the usual polycrystalline INCO600. This is due to the presence

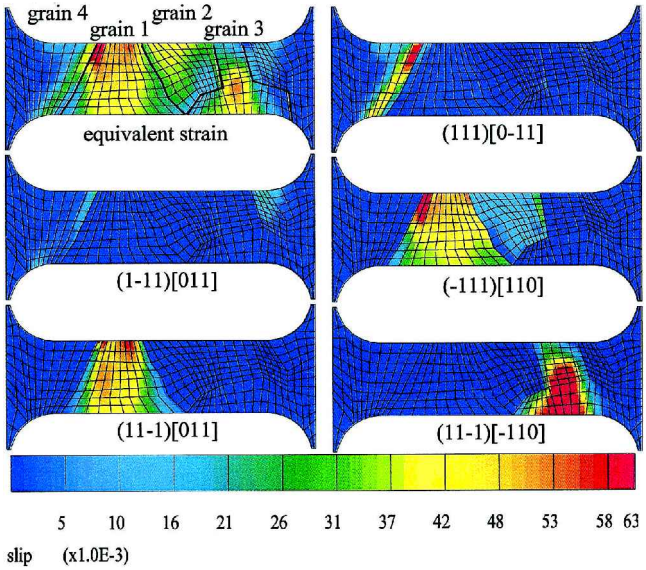

Fig. 7—Comparison of the equivalent strain at 2 pct overall strain with the main activated slip systems.

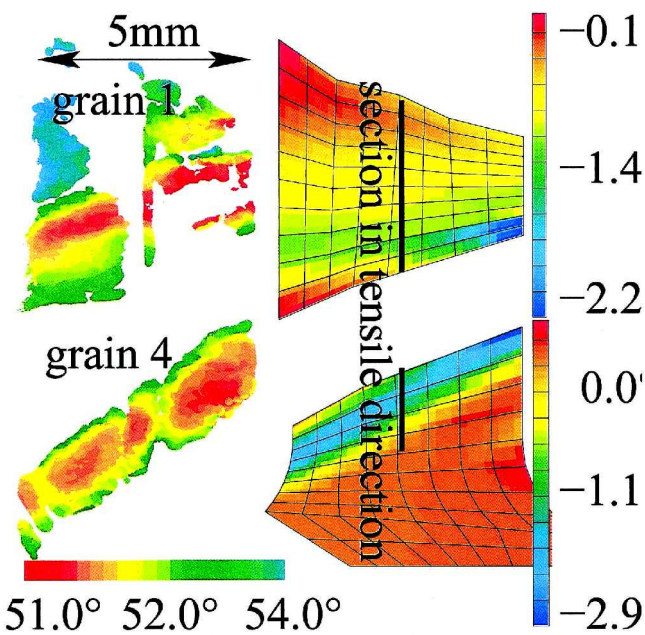

Fig. 8—Experimental orientation maps (absolute Ω position of goniometer, on the left) and the computed lattice rotation maps (rotation angle of plane normal, in degree, on the right) in grains 1 and 4. A quantitative comparison is shown in Fig. 9 along the two black vertical lines drawn on the grains.

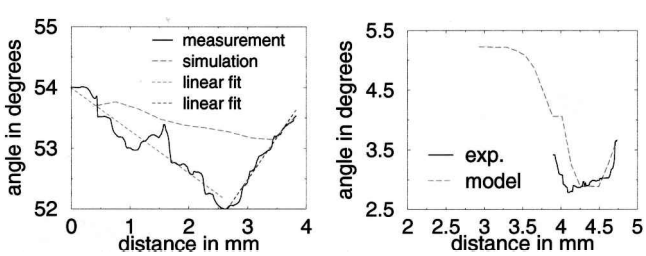

Fig. 9—Lattice orientation profiles along the lines of Fig. 8 in grains 1 (left) and 4 (right): experimental and computed results.

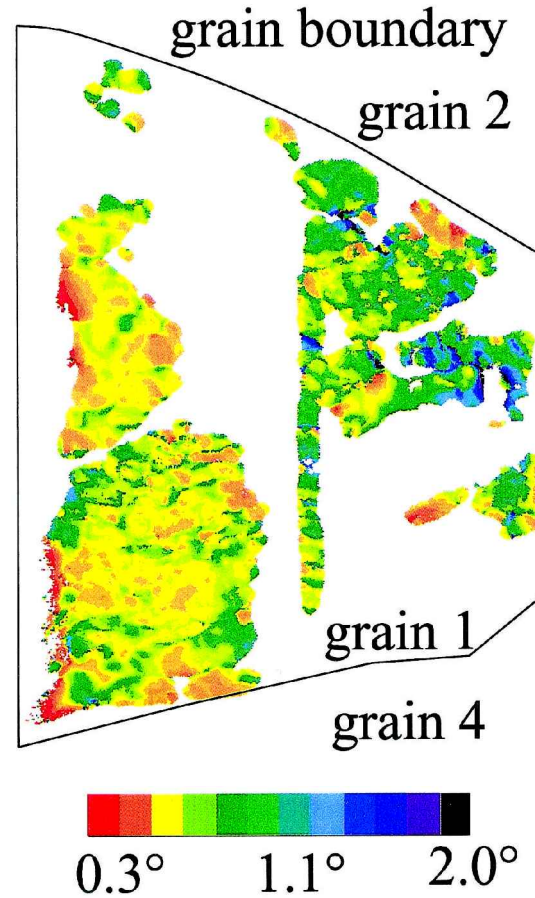

Fig. 10—Mosaicity distribution after straining in grain 1 represented by the broadening of the Ω scan in the reciprocal space mapping (observed crystallographic plane: $(3\bar{5}1)$).

of very large grains and to the fact that localization occurs in one band in grain 4. The agreement between the two curves confirms that the identification of the material parameters (from another specimen, presented in Reference 5) is correct. The mean stress component in the tensile direction has been computed for grains 1 through 4. Grains 1 and 2 have a similar orientation and show similar stress levels in the tensile direction. However, grain 1 deforms more than grain 2. This indicates complex stress states in these grains, especially in grain 2, which does not cross the entire section. The same holds for the pair (grains 3 and 4).

The information provided by the computation also concerns local slip activity. The amounts of slip for the systems mainly active in grains 1 through 4 are given in Figure 7. Even though the overall strain is 2 pct, values of 6 pct slip can be reached locally. Comparison with experimental observations is drawn in the discussion. Lattice rotation maps inside the grains can also be plotted, as in Figure 8, and compared to the experimental ones.

V. DISCUSSION

The comparison between experimental observations and measurements and numerical predictions can be made for two different issues: determination of active slip systems and analysis of lattice rotation fields.

A. *Slip-System Activity*

The activated slip systems observed in the individual grains have been analyzed in Section IV–B. They can now be compared with the numerical prediction given in Figure 7. Good agreement between the experimentally observed and the numerically calculated slip systems is reached. Even the geometrical distribution of slip can be well reproduced by the numerical simulation, as in grain 4. The existence of double slip in grain 1 is confirmed. The absence of slip traces in grain 2 is in agreement with the small amounts of plastic strain computed. Locally multiaxial stress states are predicted by the simulation, but they are not reported in detail here, since it is not the main topic of the article. An intense deformation band is predicted in grain 4 by the finite-element analysis. It is confirmed by the experimental observation.

B. *Lattice Rotation Fields*

Here, the crystallographic curvature of grains 1 and 4 is considered more precisely. In order to obtain a large number of crystallographic planes, a plane family with three different Miller indices was chosen; the lowest possible which satisfies the diffraction condition for fcc materials is the {531} plane family. The resulting Bragg angle of about 52 deg is the maximum angle possible of the experimental setup without shadowing the incident beam. A large Bragg angle was chosen to orient the sample as straight as possible in front of the CCD camera. The crystallographic planes, $(5\bar{1}3)$ for grain 4 and $(3\bar{5}\bar{1})$ for grain 1, were chosen with low tilt angles (Ψ) to avoid large projection angles. The camera records only the projection of the grain on the observation plane defined by the camera. The images have to be transformed in the camera plane to obtain the real grain size and to superpose images acquired from different tilt orientations.

Due to this transformation into the camera plane, the pixels are stretched and the pixel resolution of the camera of 12×12 μm, mentioned in Section III, cannot be maintained for the image exploitation. On average, the resolution becomes 30×30 μm. The results presented in Figure 8 show the grain-transformed image, *i.e.*, the real undistorted grain.

Figure 8 represents the Ω angle as a function of the pixel in grains 1 and 4, obtained by the two-dimensional Gauss-fit method at a 2 pct overall strain of the multicrystal. The angle Ω corresponds to the goniometer orientation, so that at fixed Ψ and ϕ angles, Ω can be directly identified with the lattice orientation of the measured (*hkl*) plane normal around the Ω axis. The absolute values of Ω are given. The difference between 51 to 54 deg only is of interest here. This variation with amplitude of about 3 deg can be compared to the values calculated by the finite-element method represented on the right-hand side of Figure 8. In both grains, a diagonal band crossing the entire specimen width can be observed. At the center of the band, the highest Ω angle can be observed, and at both sides of the band, the angle is decreasing, so that the crystallographic lattice can be imagined as an S-shaped curvature, where the change in the curvature orientation is at the highest Ω angle.

In order to compare the experimental measurements with the numerical calculations, the orientation vector of the crystallographic lattice has to be projected in the concerned measurement direction. The observed planes in Figure 8 for grains 1 and 4 were, respectively, $(3\bar{5}\bar{1})$ and $(5\bar{1}3)$. Their orientation variations are compared with the numerical simulation, and a good agreement is found. A quantitative comparison is done on the right-hand side of Figure 9: the values along the black lines, in the tensile direction near the center of the grain (Figure 8), are compared for the model and experiment. The rotation of the lattice-plane normal, $(3\bar{5}\bar{1})$ in grain 1 and $(5\bar{1}3)$ in grain 4, is presented as a function of the distance from the grain center to the grain boundary in grain 4 and through the entire grain in grain 1.

Very good agreement can be found in grain 4, where the strain band is not only confirmed for the plastic deformation, but also for the lattice orientation. The tendency of grain 1 is confirmed as well, even if the model underestimates the rotation of the crystallographic lattice.

This underestimation can be explained by a lattice distortion already present at the initial state of the sample. High-energy Laue measurements (unpublished research) confirm this observation, showing that a rather strong subgrain splitting (*i.e.*, mosaicity, as defined in Section I) is already seen in the undeformed-state grain 1.

Finally, the lattice curvature can be estimated by a linear fit of the rotation angles as a function of the distance within the grain. In grain 1, a curvature of 1.4 deg/mm in the higher part can be compared to that of -0.7 deg/mm in the lower part.

The second order, or II' scale, as introduced in Reference 5, covers all types of heterogeneities which are taken into account by the finite-element model used with the resolution of the mesh size. Nevertheless, the model is based on continuum mechanics, so that random subgrain structures are not taken into account. Especially in grains of polycrystals or even of multicrystals, the crystalline quality can be expressed as a function of this mosaicity distribution. The mosaicity is superposed to the regular curvature of the crystal. If the two-dimensional Gauss fit is applied in the processing of the reciprocal-space maps of each pixel, the width of the peak in the Ω direction represents this random mosaic distribution of the grain. The grain is separated into zones of mosaics, as shown in Figure 10. Each color represents a Ω-peak broadening, which is distributed randomly within the grain.

VI. CONCLUSIONS AND FUTURE WORK

A finite-element model with constitutive equations based on Schmid's law has been applied to the simulation of a tensile test on a multicrystalline sample. It has been validated at the scale of individual grains concerning the lattice rotation field. A new experimental approach allows the acquisition of the entire grain with its detailed heterogeneous lattice-orientation distribution. The use of synchrotron radiation with a two-dimensional detector guarantees a parallel beam configuration, but requires complex data processing.

The crystalline curvature based on continuum mechanics has been predicted in localized zones like the strain band in grain 4. The effects of random mosaicity and regular crystallographic curvature could be distinguished and processed separately.

In a multicrystalline sample with an overall strain of 2 pct and a local strain within the grain up to 6 pct, a lattice curvature of about 1.4 deg/mm has been found. An average mosaic distribution with an orientation spread of ± 0.5 deg

is superposed to the regular crystallographic curvature. The mosaicity can be considered as a background phenomenon.

An important part of the information provided by the synchrotron experiment was not used in this work. This concerns the interpretation of the peak position and peak broadening in the Ω - 2θ orientation of the reciprocal-space map for each pixel. Some preliminary results are presented in Reference 3. A more quantitative interpretation would require a higher resolution in the Ω - 2θ direction, due to the necessary high sensitivity for a correct lattice-parameter determination. This would provide a complete elastic-strain field in addition to the already-depicted orientation field. The stress field could be deduced from the elastic-strain-field measurement and compared directly to the finite-element computation.

REFERENCES

1. M. Berveiller and A. Zaoui: *J. Mech. Phys. Solids*, 1979, vol. 6, p. 326.
2. L. Méric, P. Poubanne, and G. Cailletaud: *J. Eng. Mater. Technol.*, 1991, vol. 113 pp. 162-70.
3. F. Eberl: Ph.D. Thesis, Ecole des Arts et Métiers de Paris, Paris, 1999.
4. A.-F. Gourgues, E. Andrieu, P. Pilvin, and P. Scott: in *Corrosion-Deformation Interactions '96*, The Institute of Materials, London 1997, pp. 453-62.
5. F. Eberl, G. Cailletaud, and J.-L. Lebrun: *Proc. Adv. in X-Ray Anal.*, 1998, vol. 42, pp. 116-21.
6. A.J. Schwartz: *Electron Backscatter Diffraction in Materials Science*, Kluwer Academic/Plenum Publishers, New York, NY, 2001.
7. F. Delaire, J.L. Raphanel, and C. Rey: *Acta Mater.*, 2000, vol. 48, pp. 1075-87.
8. R. Parisot, S. Forest, A.-F.Gourgues, A. Pineau, and D. Mareuse: *Computat. Mater. Sci.*, 2001, vol. 19, pp. 189-204.
9. S. Forest: *Acta Mater.*, 1998, vol. 9, pp. 3265-81.
10. J. Mandel: *Int. J. Solids Struct.*, 1973, vol. 9, pp. 725-40.
11. R.J. Asaro: *J. Appl. Mech.*, 1983, vol. 50, pp. 921-34.
12. A. Needleman, R.J. Asaro Asaro, J. Lemonds, and D. Peirce: *Comp. Meth. Appl. Mech. Eng.*, 1985, vol. 52, pp. 689-708.
13. C. Teodosiu, J.L. Raphanel, and L. Tabourot: in *Large Plastic Deformations*, MECAMAT '91, C. Teodosiu and F. Sideroff, eds., Balkema, Rotterdam, The Netherlands, 1993.
14. S. Forest and P. Pilvin: *Z. Angew. Math. Mech.*, 1999, vol. 79, pp. 199-202.
15. J. Mandel: *J. Méc. Théor. Appl.—1*, 1982, vol. 1, pp. 7-23.
16. L. Méric, G. Cailletaud, and M. Gaspérini: *Acta Metall.*, 1994, vol. 42, pp. 921-35.
17. F. Eberl, F. Feyel, S. Quilici, and G. Cailletaud: *J. Phys. IV France*, 1998, vol. 8, pp. 15-25.
18. T. Wroblewski, D. Breuer, H.A. Crostack, F. Fandrich, M. Gross, and P. Klimanek: in *European Powder Diffraction Proc. EPDIC5*, Trans Tech Publications, Aedermannsdorf, Switzerland, 1998, pp. 216-20.